Technical Completion Report
Project UCAL-WRC-W-942
07/01/00 - 06/30/02

Submitted to the
Water Resources Center
Centers for Water and Wildland Resources
University of California

Hydrodynamic Design in Coastal Wetland Restoration

Professor Brett F. Sanders and Dr. Feleke Arega
Department of Civil and Environmental Engineering
University of California, Irvine
(949) 824-4327

November, 2002

The research leading to this report was supported by the University of California, Water Resources Center, as part of Water Resources Center Project UCAL-WRC-W-942.

Contents

Abstract **ii**

Problem Introduction and Research Objectives **1**

Methodology **2**

Hydrodynamic Model 2

Solute Transport Model 4

Particle Transport Model 5

Computational Methods 6

Principal Findings and Significance **11**

Site Description 11

Model Calibration and Validation 11

Circulation Analysis 13

Summary and Conclusions 14

References **15**

Abstract

Coastal wetlands in California are critically positioned at the interface between increasingly developed watersheds and the coastal ocean. These wetlands provide habitat for fish and wildlife, provide nutrients to surrounding coastal waters, and create recreational opportunities (Mitsch and Gosselink 1986). This report describes a circulation and transport model that is designed for tidal wetland circulation and mixing studies. Given the importance of wetland restoration projects to offset the impact of coastal development, wetland circulation and mixing models are of great utility for evaluating the advantages and disadvantages of various wetland restoration alternatives relative to issues such as bathing water quality, eutrophication, and sedimentation. An application of the model to a restored wetland and guidelines for its use are presented.

Key Words

Tidal wetlands, salt marsh, circulation modeling, solute transport, particle transport.

Problem Introduction and Research Objectives

Promoted by conservation-banking practices initiated in 1995, wetland restoration and enhancement projects have emerged in southern California as the primary means to mitigate the impact of coastal development. For example, the enhancement of the Bolsa Chica wetland now underway in Huntington Beach is tied to the expansion of the Ports of Los Angeles and Long Beach. Constructed wetlands reclaim habitat for fish and wildlife, provide nutrients to surrounding coastal waters, mitigate the impact of pollutants in urban runoff, and create recreational opportunities (Mitsch and Gosselink 1986).

Successful enhancement and restoration designs hinge on a reliable prediction of physical processes including flow, circulation, and transport of nutrients, salinity, sediments, and pollutants. A poor prediction can cause a design to fail. Talbert Marsh in Huntington Beach serves as an excellent example. It was constructed in 1990, but by 1991 the marsh had yet to achieve the intertidal zone of the design. By 1995, longshore sediment-transport led to a partial blocking of the Marsh outlet, sedimentation lead to 4-6 feet of silt on the marsh bottom, and the expected level of diversity had not materialized (Jones & Stokes 1997).

Engineers use both physical and numerical models to evaluate different wetland restoration plans. Factors typically predicted by models include rates of accretion, potential for scour as a result of either watershed runoff or storm surge, distributions of residence times, and velocity and/or shear regimes, to name a few.

This report presents a new flow and transport model that is designed specifically for tidal wetlands but is sufficiently generic to accommodate a wide range of site specific investigations into topics such as bathing water quality, eutrophication, and sedimentation. The model solves depth averaged continuity, momentum, and solute transport equations using the finite volume method, and it also includes a three dimensional particle transport module. The model accounts for flooding and draining of intermittently wetted areas such as mudflats, it has excellent conservation properties, and it is non-oscillatory which in practical terms means that it will not erroneously predict negative solute concentrations or artificially increase solute predictions, even at the wet/dry interface. This feature may be particularly important in bathing water quality studies, where fecal indicator bacteria predictions must be accurate over several log units. Researchers interested in using this model should contact Professor Sanders.

Methodology

Hydrodynamic Model

Circulation predictions are made by solving the integral form of the shallow water equations,

$$\frac{\partial}{\partial t}\int_\Omega \mathsf{U} d\Omega + \oint_{\partial\Omega} (\mathsf{F}dy - \mathsf{G}dx) = \int_\Omega \mathsf{S} d\Omega \tag{1}$$

where $\mathsf{U} = (h \quad h\bar{u} \quad h\bar{v})^T$ and

$$\mathsf{F} = \begin{pmatrix} h\bar{u} \\ h\bar{u}^2 + \frac{1}{2}g^* h^2 - h(T_{uu} + D_{uu}) \\ h\bar{u}\bar{v} - h(T_{uv} + D_{uv}) \end{pmatrix} \qquad \mathsf{G} = \begin{pmatrix} h\bar{v} \\ h\bar{u}\bar{v} - h(T_{uv} + D_{uv}) \\ h\bar{v}^2 + \frac{1}{2}g^* h^2 - h(T_{vv} + D_{vv}) \end{pmatrix} \tag{2}$$

$$\mathsf{S} = \begin{pmatrix} 0 \\ -g^* h\frac{\partial z_b}{\partial x} - c_D \bar{u}\sqrt{\bar{u}^2 + \bar{v}^2} + f\bar{v}h \\ -g^* h\frac{\partial z_b}{\partial y} - c_D \bar{v}\sqrt{\bar{u}^2 + \bar{v}^2} - f\bar{u}h \end{pmatrix} \tag{3}$$

The term h represents the flow depth, while $\bar{u}$ and $\bar{v}$ are the vertically-averaged velocities in the x and y directions, respectively. The gravitational term g^* is given by

$$g^* = g(1 + \Delta\rho/\rho_o) \tag{4}$$

where ρ_o is a reference density, $\Delta\rho = \rho - \rho_o$, ρ represents the average fluid density over the depth and g is the gravitational constant, so the model is consistent with the Boussinesq approximation whereby density variations are only resolved in terms that are multiplied by the gravitational constant. The parameter f represents the Coriolis acceleration which is given as $f = 2\Omega\sin(\phi)$, where Ω is the magnitude of the angular velocity of the earth's rotation ($7.29 \times 10^{-5}\, rad/s$) and ϕ is the geographic latitude (positive being north of the equator). For most tidal wetlands, f can be assumed constant and for channelized wetlands it is unnecessary to include it in the formulation. The bed elevation above an arbitrary datum is denoted by z_b and c_D is a drag coefficient that is computed locally based on the roughness at the bed divided by the depth, k_s/h, and the Reynolds number $Re = \sqrt{\bar{u}^2 + \bar{v}^2}h/\nu$ where ν is the kinematic viscosity,

$$c_D = \begin{cases} 0.2044/\left\{\log\left[1.72/Re + (k_s/14.8h)^{1.11}\right]\right\}^2 & \text{if} \quad k_s/h < 0.2 \\ 1.56 \times 10^{-2}(k_s/h)^{1/3} & \text{if} \quad k_s/h \geq 0.2 \end{cases} \tag{5}$$

which is an adaptation of the explicit equation for the Darcy-Weisbach friction factor by Haaland (1983). If the bed roughness is known in terms of a Manning coefficient, n, then the roughness can be computed in units of meters as (Henderson 1966),

$$k_s = 0.3048\,(n/0.031)^6 \tag{6}$$

The depth averaged turbulent stresses are given by T_{uu}, T_{uv}, and T_{vv}, though elsewhere these have been written as, $\overline{\langle u'u' \rangle}$, $\overline{\langle u'v' \rangle}$, and $\overline{\langle v'v' \rangle}$, respectively. These stresses and can be interpreted

as the average over the depth (overline notation) of the ensemble average (angled bracket notation) of the product of turbulent fluctuations in the velocity field. These fluctuations correspond to differences between the instantanous point-wise velocity and the ensemble average point-wise velocity (Rodi 1984). D_{uu}, D_{uv}, and D_{vv} are dispersion terms that are defined by,

$$\begin{aligned} D_{uu} &= \frac{1}{h}\int_{z_b}^{z_b+h}(u-\bar{u})^2\,dz \\ D_{uv} &= \frac{1}{h}\int_{z_b}^{z_b+h}(u-\bar{u})(v-\bar{v})\,dz \\ D_{vv} &= \frac{1}{h}\int_{z_b}^{z_b+h}(v-\bar{v})^2\,dz \end{aligned}$$

where u and v correspond to point-wise velocities. Both the turbulence stresses and dispersion stresses are small in comparison to the depth-averaged hydrostatic and intertial fluxes, as well as the shear stress at the bed, and often these terms are omitted from circulation models without loss of accuracy. In tidal environments, there may be cases where lateral shear is important relative to the circulation, such as at a harbor entrance. Flow passing through a constriction and into a larger body of water can act like a jet, creating eddies on either side. Without a viscous-like term in the governing equations, numerical predictions of these eddies will not be reliable because there is no real viscosity in the model, only numerical viscosity. Consequently, in this model turbulent stresses are included using an eddy viscosity model (Rodi 1984),

$$T_{uu} = 2\nu_t\left(\frac{\partial\bar{u}}{\partial x}\right) - \frac{2}{3}k, \quad T_{uv} = \nu_t\left(\frac{\partial\bar{u}}{\partial y} + \frac{\partial\bar{v}}{\partial x}\right), \quad \text{and} \quad T_{vv} = 2\nu_t\left(\frac{\partial\bar{v}}{\partial y}\right) - \frac{2}{3}k \qquad (7)$$

where ν_t is the eddy viscosity and $\bar{k} = (\overline{u^2+v^2})/2$ is the kinetic energy of the fluctuating velocities, averaged over the depth. The dispersion terms are not included because, in the absence of secondary currents, these terms will simply enhance the transfer of momentum in the direction of flow which will not help to better resolve eddies.

Resolving the eddy viscosity is a classic problem in turbulence modeling for which there are many solution approaches, none of which has received universal acceptance. A good summary of options is given by (Bedford *et al.* 1988). In the context of a depth-averaged model, the eddy viscosity can be related to the transerse mixing coefficient ε_t through the Schmidt number σ_t which represents the ratio of momentum and mass transport rates,

$$\sigma_t = \nu_t/\varepsilon_t \qquad (8)$$

and experiments have shown that the Schmidt number is unity in shear flow boundary layers (Fischer *et al.* 1979). Studies of pollutant transport have shown that ε_t is correlated to the shear velocity and depth as follows,

$$\varepsilon_t = \beta u^* h \qquad (9)$$

where $u^* = \sqrt{\tau_o/\rho_o}$ and β varies in the range of 0.1-0.8 depending on the channel geometry (Fischer *et al.* 1979). Smaller values of β have been reported for smooth flumes, while larger values have been reported for natural channels. According to Fischer *et al.* (1979), $\beta = 0.6 \pm 50\%$

is typical of natural channels. Using the drag coefficient c_D which is resolved using Eq. 5, the shear velocity is estimated as $u^* = \sqrt{c_D(\bar{u}^2 + \bar{v}^2)}$, and estimation of ε_t is accomplished using Eq. 9 while estimation of ν_t is accomplished using Eq. 8. This approach to turbulent closure is attractive for several reasons. First, it requires little computational effort compared to other approaches that require the solution to additional transport equations. Second, it leads to a spatially and temporally varying eddy viscosity which has been found to be necessary to achieve reasonable flow predictions. Third, it facilitates solute and particle transport predictions. There are clearly limitations to this model. For example, it should only be applied in applications where turbulence is generated by the bed, so it should not be applied to vertically stratified flow problems, for reasons not limited to the fact that turbulence may be generated at the pycnocline, or to problems involving jets or buoyant plumes. However, it is reasonable for many tidal wetlands in California characterized by depths of only a few meters and forced primarily by the tide and secondarily by watershed runoff and possibly the wind.

Solute Transport Model

Dissolved scalars are modeled by solving depth-averaged transport equations that account for advection, turbulent diffusion, dispersion, and source and sink terms. These equations appear as,

$$\frac{\partial}{\partial t}\int_\Omega \mathsf{Q}\, d\Omega + \oint_{\partial\Omega} (\mathsf{F}_\mathsf{Q}\, dy - \mathsf{G}_\mathsf{Q}\, dx) = \int_\Omega \mathsf{S}_\mathsf{Q}\, d\Omega \tag{10}$$

where $\mathsf{Q} = (hc_1 \quad hc_2 \quad \dots \quad hc_N)^T$ and

$$\mathsf{F}_\mathsf{Q} = \begin{pmatrix} h\bar{u}c_1 - h(T_{uc_1} + D_{uc_1}) \\ h\bar{u}c_2 - h(T_{uc_2} + D_{uc_2}) \\ \vdots \\ h\bar{u}c_N - h(T_{uc_\mathrm{N}} + D_{uc_\mathrm{N}}) \end{pmatrix} \mathsf{G}_\mathsf{Q} = \begin{pmatrix} h\bar{v}c_1 - h(T_{vc_1} + D_{vc_1}) \\ h\bar{v}c_2 - h(T_{vc_2} + D_{vc_2}) \\ \vdots \\ h\bar{v}c_N - h(T_{vc_\mathrm{N}} + D_{vc_\mathrm{N}}) \end{pmatrix} \mathsf{S}_\mathsf{Q} = \begin{pmatrix} s_1 \\ s_2 \\ \vdots \\ s_N \end{pmatrix} \tag{11}$$

where c_j corresponds to the depth-averaged concentration of the j^{th} dissolved scalar, T accounts for turbulent diffusion, D accounts for dispersion, and s_j is a general source/sink term that can also include terms accounting for reactions between solutes. Turbulent diffusion accounts for mass transfer due to turbulent fluctuations in the point-wise values of both the velocity and the solute, while dispersion is an artifact of the depth averaging process. Physically, dispersion accounts for mass transfer due to dissolved molecules at the surface moving faster than dissolved molecules at the bed. This process was documented first in turbulent pipe flow (Taylor 1954), and later for turbulent shear flows (Elder 1959). Whereas turbulent diffusion acts in all directions, dispersion only acts in the direction of the local velocity which we call the longitudinal direction. Elder (1959) showed that the sum of turbulent diffusion and dispersion in the longitudinal direction is given by,

$$T_{u_\mathrm{l}c_\mathrm{j}} + D_{u_\mathrm{l}c_\mathrm{j}} = \varepsilon_l \frac{\partial c_j}{\partial s} \tag{12}$$

where s represents the longitudinal direction, u_l is the depth-averaged velocity in the longitudinal

direction, and $\varepsilon_l = 5.93\, u^* h$. Turbulent diffusion in the transerve direction is given by,

$$T_{u_t c_j} = \varepsilon_t \frac{\partial c_j}{\partial n} \tag{13}$$

where n represents the transverse direction, u_t is the depth-averaged velocity in the transverse direction, and ε_t is given by Eq. 9. The turbulence and dispersion terms in Eq. 11 are subsequently resolved as follows,

$$T_{uc_j} + D_{uc_j} = \varepsilon_{uu} \frac{\partial c_j}{\partial x} + \varepsilon_{uv} \frac{\partial c_j}{\partial y} \tag{14}$$

$$T_{vc_j} + D_{vc_j} = \varepsilon_{uv} \frac{\partial c_j}{\partial x} + \varepsilon_{vv} \frac{\partial c_j}{\partial y} \tag{15}$$

where

$$\begin{aligned} \varepsilon_{uu} &= \varepsilon_t + (\varepsilon_l - \varepsilon_t) \frac{\bar{u}^2}{\bar{u}^2 + \bar{v}^2} \\ \varepsilon_{uv} &= (\varepsilon_l - \varepsilon_t) \frac{|\bar{u}\bar{v}|}{\bar{u}^2 + \bar{v}^2} \\ \varepsilon_{vv} &= \varepsilon_t + (\varepsilon_l - \varepsilon_t) \frac{v^2}{\bar{u}^2 + \bar{v}^2} \end{aligned} \tag{16}$$

This formulation for the Reynolds fluxes assumes that predictions are of interest on a time scale that is longer than the Lagrangian time scale (Fischer 1979), meaning that the position of a molecule in the water column at time t is not correlated to its position at time $t + t_{\mathcal{L}}$, where $t_{\mathcal{L}}$ is the Lagrangian time scale. In practical terms, this means that molecules are vigorously mixed over the depth. Such conditions are often found in tidal wetlands, where the tide advancing over shallow depths causes rapid mixing in the vertical. Wetland areas sheltered from tidal action may constitute an exception, and these may develop periodically as a function of fortnightly lunar cycles, which modulate the peak stages of the tide, or by diurnal or semidiurnal cycles, whereby portions of a wetland become disconnected from the main channel at low tide after land bridges are exposed.

Recalling that the hydrodynamic formulation includes variations in the depth-averaged fluid density, consistent with the Boussinesq approximation, the solute transport model can be used to track variations in salinity, temperature, or both so that the fluid density can be estimated using an equation of state of the form $\rho = \rho(S, T)$ where S is salinity and T is temperature. Like any hydrodynamic or transport calculations, appropriate initial and boundary conditions are necessary to track these quantities and in the case of temperature, the heat exhanges at the fluid-bed and fluid-air interface due to conduction, evaporation, and/or radiation need to be parameterized.

Particle Transport Model

Particle transport is modeled by solving three-dimensional kinematic equations accounting for particle advection by the instantanenous velocity, particle settling as function of particle mass

and size, and anisotropic turbulent diffusion whereby the eddy diffusivity in the vertical ε_v is roughly an order of magnitude smaller than the transverse eddy diffusivity, ε_t. Both particle advection and turbulent diffusion processes are modeled assuming that a turbulent boundary layer extends from the bed. This gives the fluid velocity as,

$$u = f(\psi)\bar{u}, \qquad v = f(\psi)\bar{v}, \qquad w = 0, \tag{17}$$

$$f(\psi) = 1 + \frac{u*}{\kappa\sqrt{\bar{u}^2 + \bar{v}^2}}\left(1 + \log\psi\right), \tag{18}$$

$\psi = (z - z_b)/h$ and $\kappa = 0.41$, Von Karman's constant. Based on this velocity profile and a Schmidt number of unity, the vertical eddy diffusivity is given as,

$$\varepsilon_v = \kappa u^* h\psi(1 - \psi) \tag{19}$$

and its depth averaged value is given by $\overline{\varepsilon_v} = \kappa u^* h/6$. While we have knowledge of the vertical variability of the vertical eddy diffusivity, we have no such knowledge of the vertical variability of the transverse eddy diffusivity, at least in the context of the present hydrodynamic and turbulent closure models. The latter has been deduced empirically.

The kinematic equations describing the position (x_p, y_p, z_p) of each particle are given by,

$$\frac{dx_p}{dt} = u + \mathcal{R}_{\mathcal{W}}(\varepsilon_t) \tag{20}$$

$$\frac{dy_p}{dt} = v + \mathcal{R}_{\mathcal{W}}(\varepsilon_t) \tag{21}$$

$$\frac{dz_p}{dt} = -W_s + \mathcal{R}_{\mathcal{W}}(\overline{\varepsilon_v}) \tag{22}$$

where $\mathcal{R}_{\mathcal{W}}$ is a stochastic function that induces a random-walk that is scaled by the amplitude of its argument, either ε_t or $\overline{\varepsilon_v}$. Since $\varepsilon_t \approx 10^1\overline{\varepsilon_v}$, the random walk distance of particles in the horizontal plane is, on average, an order of magnitude larger than the random walk distance of particles in the vertical direction.

Computational Methods

The finite volume method is used to solve the hydrodynamic and solute transport models. The scheme closely follows the development presented by Bradford and Katopodes (1999) and Bradford and Sanders (2002). The model is second-order accurate in space and time and it uses an explicit two-step time integration approach. The spatial domain is divided into quadrilateral computational cells, cell-average values of U are stored at the center of each cell, and fluxes are computed at the four faces that border each cell. The solution is advanced from the n to $n+1/2$ time level in a predictor step, fluxes are computed at cell faces at the $n + 1/2$ time level, and then the solution is advanced from the n to the $n + 1$. The predictor step solves the primitive form of the equations in generalized coordinates in cell j, k as

$$h_{j,k}^{n+1/2} = h_{j,k}^{n} - \frac{\Delta t}{2}\left(\bar{u}_\xi\overline{\Delta_\xi h} + \bar{u}_\eta\overline{\Delta_\eta h} + h(\xi_x\overline{\Delta_\xi\bar{u}} + \xi_y\overline{\Delta_\eta\bar{u}} + \eta_x\overline{\Delta_\xi\bar{v}} + \eta_y\overline{\Delta_\eta\bar{v}})\right)_{j,k}^{n} \tag{23}$$

$$\bar{u}_{j,k}^{n+1/2} = \bar{u}_{j,k}^{n} - \frac{\Delta t}{2}\Big(\bar{u}_\xi \overline{\Delta_\xi \bar{u}} + \bar{u}_\eta \overline{\Delta_\eta \bar{u}} + g(\xi_x \overline{\Delta_\xi \zeta} + \eta_x \overline{\Delta_\eta \zeta}) + (\xi_x \Delta_\xi T_{uu} + \eta_x \Delta_\eta T_{uu}) + (\xi_y \Delta_\xi T_{uv} + \eta_y \Delta_\eta T_{uv}) - c_D \bar{u}\sqrt{\bar{u}^2 + \bar{v}^2}/h + f\bar{v} \Big)_{j,k}^{n} \quad (24)$$

$$\bar{v}_{j,k}^{n+1/2} = \bar{v}_{j,k}^{n} - \frac{\Delta t}{2}\Big(\bar{u}_\xi \overline{\Delta_\xi \bar{v}} + \bar{u}_\eta \overline{\Delta_\eta \bar{v}} + (\xi_y \overline{\Delta_\xi \zeta} + \eta_y \overline{\Delta_\eta \zeta}) + (\xi_x \Delta_\xi T_{uv} + \eta_x \Delta_\eta T_{uv}) + (\xi_y \Delta_\xi T_{vv} + \eta_y \Delta_\eta T_{vv}) - c_D \bar{v}\sqrt{\bar{u}^2 + \bar{v}^2}/h - f\bar{u} \Big)_{j,k}^{n} \quad (25)$$

where ξ and η are in the directions of contiguous j and k indices, respectively, and the terms ξ_x, ξ_y, η_x, and η_y are the grid transformation metrics. They are computed by assuming a linear mapping of x and y onto ξ and η, which are assumed to vary from 0 to 1 in each computational cell. Also, Δt is the time step, $\zeta = h + z_b$ is the free surface elevation, $\bar{u}_\xi = \bar{u}\xi_x + \bar{v}\xi_y$, and $\bar{u}_\eta = \bar{u}\eta_x + \bar{v}\eta_y$.

The $\overline{\Delta}$ in Eqs. (23), (24), and (25) denotes cell-average gradients of the variables in the ξ and η directions. Flux or slope limiting is used when computing the gradients in order to preserve the monotonicity of the solution. The Double Minmod limiter is used when computing gradients in the velocity and free surface. For example, gradients of u in the ξ direction are computed as

$$\overline{\Delta \bar{u}} = \begin{cases} sign(a)min(|a+b|/2, 2|a|, 2|b|) & ab > 0 \\ 0 & ab \leq 0 \end{cases} \quad (26)$$

where $a = \bar{u}_{j,k} - \bar{u}_{j-1,k}$ and $b = \bar{u}_{j+1,k} - \bar{u}_{j,k}$. Analogous expressions can be deduced for the gradients in the η direction. For problems involving variable bathymetry, the spatial variation of h is often much greater than the variation of ζ. Consequently, computing $\overline{\Delta h}$ can introduce excessive numerical dissipation into the solution. Therefore, $\overline{\Delta \zeta}$ is first computed using Eq. (26) and $\overline{\Delta h} = \overline{\Delta \zeta} - \Delta z$ is then computed. Note that Δz is the non-limited change in bed elevation in the direction of $\overline{\Delta h}$.

Predicted values to the left and right of each cell face are linearly reconstructed using the Monotone Upstream Scheme for Conservation Laws (MUSCL) to obtain second order spatial accuracy. The fluxes perpendicular to each cell face are then evaluated using Roe's Godunov-type upwind scheme in which a Riemann problem is solved across each cell face. The flux $\mathsf{F}_\perp$ is positive in the direction of increasing computational coordinates, perpendicular to the cell boundary, and defined as

$$\mathsf{F}_\perp = \begin{pmatrix} h\bar{u}_\perp \\ h\bar{u}\bar{u}_\perp + \frac{1}{2}gh^2\cos\phi \\ h\bar{v}\bar{u}_\perp + \frac{1}{2}gh^2\sin\phi \end{pmatrix} + \begin{pmatrix} 0 \\ \frac{1}{12}g(\Delta_s h)^2\cos\phi \\ \frac{1}{12}g(\Delta_s h)^2\sin\phi \end{pmatrix} + \begin{pmatrix} 0 \\ hT_{uu}\cos\phi + hT_{uv}\sin\phi \\ hT_{uv}\cos\phi + hT_{vv}\sin\phi \end{pmatrix} \quad (27)$$

where $\bar{u}_\perp$ is the velocity perpendicular to the cell face, $\Delta_s h$ represents the difference in h across the length of the face, and ϕ is the angle between the face normal vector and the x axis. The

array on the left in Eq. 27 is the standard flux computed by Roe's method, the array on the right accounts for Reynolds stresses, while the array in the middle is a correction term that is necessary to preserve stationary solutions (Bradford and Sanders 2002).

Once the fluxes are computed, the corrector step follows as,

$$\frac{\mathsf{U}_{j,k}^{n+1}-\mathsf{U}_{j,k}^{n}}{\Delta t}+\frac{1}{\Omega_{j,k}}[(\mathsf{F}_{\perp}^{n+1/2}s)_{j+1/2,k}-(\mathsf{F}_{\perp}^{n+1/2}s)_{j-1/2,k}+ (\mathsf{F}_{\perp}^{n+1/2}s)_{j,k+1/2}-(\mathsf{F}_{\perp}^{n+1/2}s)_{j,k-1/2}]=\mathsf{S}_{j,k}^{n+1/2} \tag{28}$$

where U and S are assumed to be cell-average values, while $\mathsf{F}_{\perp}$ is assumed to be an average value on each cell face. Ω is the area of the cell and s is the cell face length. The integral over the cell of the source terms is resolved by evaluating the source terms at the cell center and multiplying by the area of the cell, except in the case of the bed slope terms. These are resolved using finite element bilinear shape functions to represent h and z within the cell and applying 2×2 Gauss quadrature to evaluate the integral. The hydrostatic correction to the cell face fluxes and the Gauss quadrature integration of the bed slope terms ensure that the model preserves stationarity.

Wet/Dry Boundary Tracking

Tracking the wet/dry boundary is particularly challenging. Near the wet/dry boundary, the quadrilateral cells may be completely wetted (4 submerged nodes), partially wetted (1-3 submerged nodes), or dry (0 submerged nodes). A wet node is defined by a depth greater than $10^{-6}\ m$. Nodes are the vertexes of cells, not the cell centers where the solution is stored. The general strategy adopted here is to solve the continuity equation in all cells, but only solve the momentum equation in completely wetted cells and for the other cells, set the velocity to zero. This methodology involves two components. First, the variable reconstruction process is modified at the interface between completely wetted and either partially wetted or dry cells. When the free surface elevation of the wet cell is greater than the elevation of the dry cell's bed at its cell center, variable reconstruction proceeds in the standard fashion, keeping in mind that velocities on the dry side are by definition zero. However, when this condition is not met, the reconstructed depth on the dry side of the cell face is set equal to that on the wet side, and the reconstructed velocities on the wet side of the cell face are set to zero. Second, after each corrector step a check is made for cells with a negative depth. These cells supplied more water to their neighbors than was contained in storage, so the magnitude of each volumetric flux out of the cell is reduced in proportion to the magnitude of each as well as the deficit in the dry cell. This adjustment increases the storage in the dry cell to exactly zero and reduces the storage of neighboring cells in proportion to the adjustment in the volumetric fluxes. No adjustment to the momentum of the neighboring cells is made. After this adjustment, the primitive variables $\bar{u}$, and $\bar{v}$ are computed from the conservative variables $h\bar{u}$ and $h\bar{v}$ in cells where $h > 1\ cm$. Otherwise, the velocities are set to zero.

Solute Transport

Solute transport predictions are made using the same computational grid, time levels, and predictor-corrector scheme as the hydrodynamic predictions. The predictor solution is computed by solving the primitive form of the equations in generalized coordinates in cell j,k as,

$$\begin{aligned}(c_i)_{j,k}^{n+1/2} &= (c_i)_{j,k}^{n} - \frac{\Delta t}{2}\Big(\bar{u}_\xi \overline{\Delta_\xi c_i} + \bar{u}_\eta \overline{\Delta_\eta c_i} \\ &+\xi_x \Delta_\xi (T_{uc_i} + D_{uc_i}) + \eta_x \Delta_\eta (T_{uc_i} + D_{uc_i}) \\ &+\xi_y \Delta_\xi (T_{vc_i} + D_{vc_i}) + \eta_y \Delta_\eta (T_{vc_i} + D_{vc_i}) - s_i\Big)_{j,k}^{n} \end{aligned} \tag{29}$$

where the $\overline{\Delta}$ again indicates the use of limited slopes to preserve monotonicity. In this case, the Superbee slope limiter is used,

$$\overline{\Delta c_i} = \begin{cases} sign(a)\, min[\, max(|a|,|b|),\, 2\; min(|a|,|b|)] & ab > 0 \\ 0 & ab \leq 0 \end{cases} \tag{30}$$

where $a = (c_i)_{j,k} - (c_i)_{j-1,k}$ and $b = (c_i)_{j+1,k} - (c_i)_{j,k}$ for the ξ direction. Predicted values of c are linearly reconstructed using MUSCL to obtain second order spatial accuracy. The advective and diffusive fluxes at each cell face are evaluated separately and then summed together at each cell face. The corrector solution is then updated as,

$$\begin{aligned}\frac{\mathsf{Q}_{j,k}^{n+1} - \mathsf{Q}_{j,k}^{n}}{\Delta t} + \frac{1}{\Omega_{j,k}}[(\mathsf{F}_{\mathsf{Q}\perp}{}^{n+1/2} s)_{j+1/2,k} - (\mathsf{F}_{\mathsf{Q}\perp}{}^{n+1/2} s)_{j-1/2,k} + \\ (\mathsf{F}_{\mathsf{Q}\perp}{}^{n+1/2} s)_{j,k+1/2} - (\mathsf{F}_{\mathsf{Q}\perp}{}^{n+1/2} s)_{j,k-1/2}] = \mathsf{S}_{\mathsf{Q}}{}_{j,k}^{n+1/2}\end{aligned} \tag{31}$$

The flux $\mathsf{F}_{\mathsf{Q}\perp}$ is positive in the direction of increasing computational coordinates, perpendicular to the cell boundary, and defined as

$$\mathsf{F}_{\mathsf{Q}\perp} = \begin{pmatrix} h\bar{u}_\perp c_1 + h(T_{uc_1} + D_{uc_1})\cos\phi + h(T_{vc_1} + D_{vc_1})\sin\phi \\ h\bar{u}_\perp c_2 + h(T_{uc_2} + D_{uc_2})\cos\phi + h(T_{vc_2} + D_{vc_2})\sin\phi \\ \vdots \\ h\bar{u}_\perp c_N + h(T_{uc_N} + D_{uc_N})\cos\phi + h(T_{vc_N} + D_{vc_N})\sin\phi \end{pmatrix} \tag{32}$$

The advective fluxes are evaluated by multiplying the volumetric flux at the cell face $\mathsf{F}_\perp(1)$ from Eq. (27) by the recontructed value of c_i on the upstream side of the face. The diffusive fluxes are evaluated by computing the turbulent diffusion tensor at the cell face based on the cell centered solution at the two neighboring cell centers, gradients of c normal to the cell face based on these two cells as well, and gradients parallel to the cell face using the four cells surrounding the cell face that only contact it with one node. At cell faces adjacent to a partially wet or dry cell, the diffusive flux is set to zero.

Particle Transport

A first order accurate explicit scheme is used to solve the equations describing particle positions, Eq. 22. The update equations appears as,

$$\begin{aligned} x_p^{n+1} &= x_p^n + \Delta t\, u^n + \mathcal{R}(0,1)\sqrt{2\varepsilon_t\, \Delta t} \\ y_p^{n+1} &= y_p^n + \Delta t\, v^n + \mathcal{R}(0,1)\sqrt{2\varepsilon_t\, \Delta t} \\ z_p^{n+1} &= z_p^n - \Delta t\, W_s + \mathcal{R}(0,1)\sqrt{2\varepsilon_v\, \Delta t} \end{aligned}$$

where $\mathcal{R}(0,1)$ is a random number sampled from a normal distribution with a mean of zero and a standard deviation of one. The point-wise velocities are estimated by linearly interpolating $\bar{u}^n$ and $\bar{v}^n$ at (x_p^n, y_p^n), based on the four nearest cell-centers, and then reconstructing the velocity profile using Eqs. 17 and 18.

When particles are incorrectly assigned a position above the free surface, they are repositioned at the free surface and when particles are incorrectly assigned a position below the bed, they are repositioned at the point just above the bed where the velocity is predicted to be zero by Eq. 18. When particles are incorrectly assigned a position outside the spatial domain of the model, they are repositioned at the center of the nearest interior cell.

Boundary Conditions

Three types of boundaries are encountered in tidal wetland circulation and transport studies: shoreline boundaries, inflow boundaries, and tidal boundaries. These boundaries are enforced using the ghost cell approach as is described elsewhere (Bradford and Katopodes 1999, Bradford and Sanders 2001).

Numerical Stability

The proposed model is nonlinear even for linear problems because flux limiters are used. However, a stability analysis of the method applied to the homogeneous scalar transport equation without flux limiting indicates that the Courant condition must be observed in each cell. Specifically, this condition is,

$$\left(\frac{|\lambda_\xi|}{l_\xi} + \frac{|\lambda_\eta|}{l_\eta}\right)\Delta t \leq 1 \tag{33}$$

where λ_ξ and λ_η are the largest eigenvalues in the ξ and η directions, respectively and l_ξ and l_ξ are the corresponding cell length scales.

Principal Findings and Significance

This model was applied to characterize circulation and mixing in the Talbert Marsh, a restored tidal marsh in Huntington Beach, and the tidally influenced flood control channels that drain into the marsh. This application of the model allowed the performance of the hydrodynamic, scalar transport, and particle transport modules to be assessed.

Site Description

The Talbert Marsh (TM) occupies roughly 10 ha of what used to be an extensive (1200 ha) tidal marsh environment (Grant *et al.* 2001). TM was created in 1990 when remnant marsh near the outlet of the Talbert Channel (TC), a flood control channel draining portions of Huntington Beach and Fountain Valley, was flooded following the removal of a levee. The TC is one of three flood control channels that drain the 3,300 ha Talbert Watershed (TW). The two others are the Huntington Beach Channel (HBC) and the Fountain Valley Channel (FVC). An overview of the site is illustrated in Figure 1, along with a contour map of the marsh topography. TM and the channels are strongly influenced by the tide. HBC has a nearly horizontal slope with a bed elevation close to mean sea level, and it remains flooded even during low tides. TC slopes at roughly 3×10^{-4} inland from its junction with HBC, it is flooded to the FVC junction at high tide (roughly 4 km), while at low tide it is flooded roughly half that distance.

The topographic data appearing in Figure 1 was obtained from several sources and then compiled into a digital elevation map (DEM) that serves as the computational grid and contains 11732 computational cells. These data sources included as-built plans for the channels obtained from the County of Orange, aerial photographs of the site, and survey data collected by UC Irvine students. The field survey focused on TM, and permitted the bed elevation to be resolved at roughly a 4×4 m resolution.

Model Calibration and Validation

The hydrodynamic component of the model was calibrated using data collected during April and May of 2000. Referring to Figure 1, water level and velocity were measured at three points in system: PCH, BRK, and AES. Velocities and water level were measured at the three monitoring stations using instrumentation mounted at the bottom of the channel. At PCH and BRK, acoustic doppler velocimeters with integrated pressure transducers were used (*Model 4250, ISCO Inc., Lincoln, NE*), while at AES, an electromagnetic velocimeter with an integrated pressure transducer was used (*Model S4, InterOcean Systems, San Diego, CA*). The S4 and 4250 velocimeters record an index velocity, which is not necessarily the average velocity. The instruments average the velocity of fluid particles located in a control volume of approximately 1 m^3 in the vicinity of the instrument, and the control volume generally does not extend across the entire channel cross section.

Using tide measurements taken in 18 m of water offshore of Huntington Beach using an electromagnetic velocimeter with an integrated pressure transducer (*Model S4, InterOcean Systems,*

San Diego, CA), the model was forced for the period of April 30-May 14, 2000 and comparisons between the measured and predicted water level were made. The turbulence stresses were not included in the momentum equations since the study site is highly channelized. Initially, the model over-predicted the elevation of the low water levels in the marsh. To correct this problem, the bed elevation at the junction of TC and the ocean was lowered. This region was not initially surveyed, and in fact the bed is highly mobile here to due sedimentation processes. By lowering the bed elevation at the outlet, the water level and velocity predictions at all of the stations improved considerably. This highlights the critical role that the outlet cross-section plays in modulating the hydrodynamics of tidal inlets.

Figures 2, 3, and 4 present comparisons between the measured and predicted water levels and velocities at all of the monitoring stations. The agreement is very good in all cases. Note that the flood period is considerably shorter than the ebb. This is caused primarily by the constriction at the outlet, where the bed elevation is above the mean lower water level of the ocean.

A dye experiment was conducted to evaluate the solute transport properties of the model. On 20/9/01 at 8:35 PDT, 50 ml of Rhodamine WT dye (20% solution) was poured onto the surface of TC at the beginning of the flood tide, and measurements of dye concentration were taken *in-situ* at several stations along TC using a fluorometer (*Seapoint Rhodamine Fluorometer, Seapoint Sensors Inc., Kingston, NH*). These stations are Brookhurst Street (BRK), Hamilton Street (HAM), Atlanta Street (ATL), and Indianapolis Street (IND) and are indicated in Figure 1.

Using tide measurements taken at NOAA gage 9410660 (off-shore of Los Angeles Harbor) to force the model, a simulation was run for one tide cycle using initial conditions that were obtained by running the model for the two previous tide cycles and saving the final solution. The parameter β was set to 0.6 as recommended by Fischer *et al.* (1979). Initially, the general shape of the dye pulses compared favorably to the model, but phase errors were present indicating that turbulent diffusion and dispersion was being accurately predicted, but the translational velocity was not. We observed that the dye pulse was reasonably predicted by the model during flood, but during ebb the model over-predicted the speed of the pulse. To improve the prediction, the Manning coefficent was modified in Talbert Channel inland of station HAM (see Figure 1). It was increased from 0.015 to 0.022 as a result of a trial and error calibration process. The fact that the friction factor preferentially reduced ebb velocities over flood velocities indicates that the balance of forces during flood is primarily between gravity and inertia, while during ebb the balance of forces is between gravity, inertia, and friction.

Figure 5 presents a comparison between the measured and predicted dye concentrations for both flood and ebb (note that the concentration scales vary between stations in Figure 5). The progress of the pulse up the channel during flood and back down the channel during ebb can be observed. The plume takes around 18 minutes to reach BRK station from the injection point at PCH, and it passes BRK station 600 minutes later during ebb. The model predicts that the peak concentration in the plume decreases over time as one would expect, though in places the field measurements indicate otherwise. While it is possible that these unusual changes in the peak concentration are due to weak vertical or cross-stream mixing that create concentration profiles, it is also possible that errors were made in calibrating the *in-situ* fluorometers. The dye signal was well below the visible range in this experiment, so a first-hand account of the dye distribution

cannot be provided.

The changes to the Manning coefficient described above altered the velocity predictions shown in Figures 2, 3, and 4 by only the slightest amount. At stations PCH, BRK, and AES, no changes could be observed visually in plots similar to Figures 2, 3, and 4.

The combination of Eulerian observations (velocity and water level meters) and Lagrangian observations (dye) proved to be an excelled means of ensuring that the hydrodynamic model accurately resolved the velocity field. A key result of this field investigation is that only calibration of the velocity field appears to be necessary to accurate predict both transport (advection) and mixing (turbulent diffusion and dispersion). That is, no calibration of the mixing properties of the model was necessary. Mixing coefficients published in the literature work very well, $\varepsilon_t = 0.6u^*h$ and $\varepsilon_l = 5.93u^*h$.

Circulation Analysis

Following the hydrodynamic and solute transport calibration of the model, the particle tracking component of the model was applied in order to develop a better understanding for the distribution of residence times throughout the Talbert system. For this analysis, the model was forced by a harmonic 1.1 m amplitude tide, which is typical of springs at the study site, and the settling velocity was set to zero (Case 1) and 0.1 cm/s (Case 2). For each case, 10 particles were placed at the center of each computational cell with ψ=0.4, where the point-wise velocity equals the mean velocity. The model was then run for a total of 12 tide cycles starting at high tide, and the position of each particle was tracked in three dimensions until it entered the ocean, at which point the time was recorded. The time that elapses between onset of the simulation and particle entry into the ocean represents the particle residence time. The mean residence time μ_t of the ten particles leaving each computational cell was subsequently computed. These residence times are contoured in Figure 6 for Case 1, which highlights regions of the system that are quickly flushed (center of marsh, lower reaches of Talbert and Huntington Beach channels), as well as regions that are slower to flush (edges of marsh, upper reaches of channel). In fact, at the end of the simulation the upper reaches of the channels still contained many particles, indicating that the flushing time exceeds 12 tide cycles or 6 days.

A histogram of residence times was computed using a bin size of 10 min, and it is presented in Figure 7 for both Case 1 (top) and Case 2 (bottom). It is clear that the majority of particles are flushed from the system in the first tide cycle, but that particles continue to be flushed over subsequent tide cycles. During all but the first ebb cycle there is a common pattern to the histogram whereby a large number of particles leave during the first part of the ebb tide, a small number of particles leave in the middle of the ebb tide, and a large number of particles leave at the end of the ebb tide. This result highlights an interesting circulation pattern whereby particles from the upper reaches of HBC and TC travel towards the outlet over the ebb, but never reach the outlet. During the flood, these particles are swept predominantly into the edges of the marsh (as opposed to back up the main channel) and on the subsequent ebb, they reach the ocean early in the ebb tide as the marsh drains. These circulation patterns may be particularly important relative to pollutant tranport because it indicates that a substantial fraction of pollutants entering the watershed (from the upstream reaches of the channel network) are cycled through Talbert

Marsh prior to entering the ocean. By characterizing the transformation processes that occur in the various marsh zones (upland, inter-tidal, sub-tidal), it may be possible to predict the overall effect of the wetland on pollutants. Conversely, it may be possible to help characterize macroscale transformation processes as a function of marsh zones by solving an inverse problem with the model. That is, the model could be used to find the macroscale transformation processes that minimize the misfit between measured and predicted pollutant levels.

Comparing Case 1 against Case 2, the settling velocity acts to increase the number of particles leaving the system at later times. It is not clear whether or not the settling velocity preferentially enhances particle transport over the ebb, or delays the flushing of particles that left in Case 1 during the first cycle. Further analysis of the particle transport data is necessary to clarify this.

Summary and Conclusions

The report presents a numerical model that is designed specifically to address circulation and mixing issues in tidal wetlands. The challenging problem of describing the inundation and drainage over intermittently wetted areas was addressed. The model requires that both an Eulerian and Lagrangian observational program be implemented in order to properly resolve the velocity field. However, no tuning of the mixing properties is required. Elder's equation for the dispersion coefficient works very well in this regard. Application of a calibrated model to a wetland system highlights interesting circulation and mixing properties.

References

Bedford, K., Findikakis, A., Larock, B.E., Rodi, W. and Street, R.L. (1988) "Turbulence Modeling of Surface Water Flow and Transport, Parts I-V., *Journal of Hydraulic Engineering*, 114(9), 970-1073.

Bradford, S.F. and Katopodes, N.D. (1999), "Hydrodynamics of Turbid Underflows Part I: Formulation and Numerical Analysis," *Journal of Hydraulic Engineering*, 125(10), pp. 1006-1015.

Bradford, S.F. and Sanders, B.F. (2002) "Finite Volume Model for Shallow-Water Flooding and Drying of Arbitrary Topography," *Journal of Hydraulic Engineering* 128(3), 289-298.

Elder, J.W. (1959) "The Dispersion of a Marked Fluid in Turbulent Shear Flow," *Journal of Fluid Mechanics*, 5, 544-560.

Fischer, H.B., List, E.J., Koh, R.C.Y., Imberger, J. and Brooks, N.H. (1979) *Mixing in Inland and Coastal Waters*, Academic Press.

Grant, S.B., Sanders, B.F., Boehm, A.B., Redman, J.A., Kim, J.H., Mrse, R., Chu, A.K., Gouldin, M., McGee, C., Gardiner, N., Jones, B.H., Svejkovsky, J., Leipzig, V., and Brown, A. (2001) "Generation of Enterococci Bacteria in a Coastal Wetland and its Impact on Surf Zone Water Quality," *Environmental Science and Technology*, 35(12), pp. 2407-2416.

Haaland, S.E. (1983) "Simple and Explicit Formulas for the Friction Factor in Turbulent Pipe Flow," *ASME Journal of Fluids Engineering*, 105, 89-90.

Henderson, F. M., (1966) *Open Channel Flow*, Macmillan.

Jones & Stokes Associates, Inc. (1997) *Talbert Marsh restoration project five-year postrestoration monitoring report. Final.* December. (JSA 96-300) Sacramento, CA. Prepared for Huntington Beach Wetlands Conservancy, Huntington Beach, CA.

Mitsch, W.J. and Gosselink, J.G. (1986) *Wetlands*, Van Nostrand Reinhold Company.

Rodi, W. (1984) *Turbulence Models and Their Application in Hydraulics - A State of the Art Review,*, IAHR, Rotterdamseweg, The Netherlands.

Taylor, G.I. (1954) *Proc. Roy. Soc. A* 223, 446.

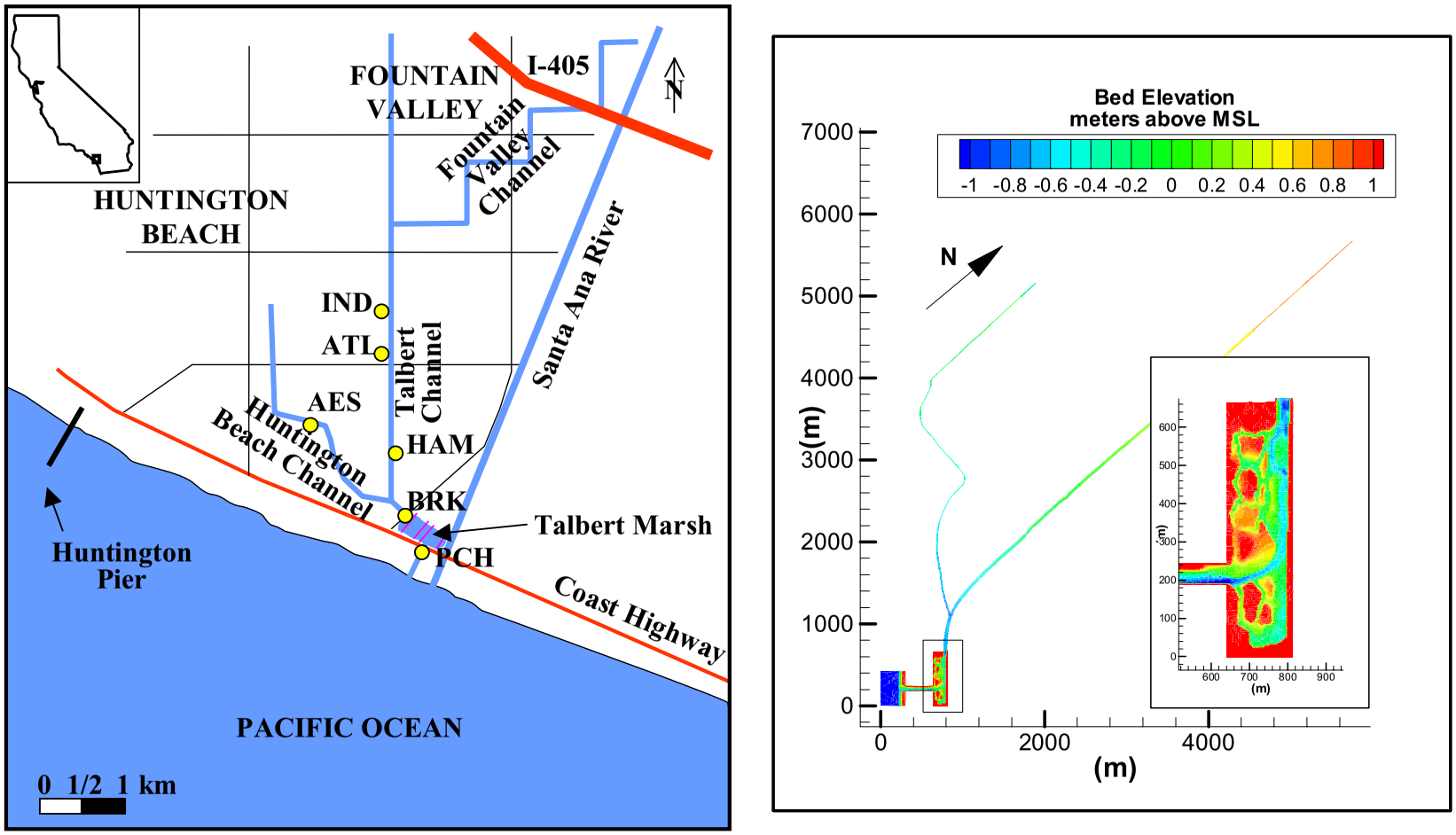

Figure 1: Talbert Watershed site map (left) and digital elevation map (right) of channels and marsh (inset).

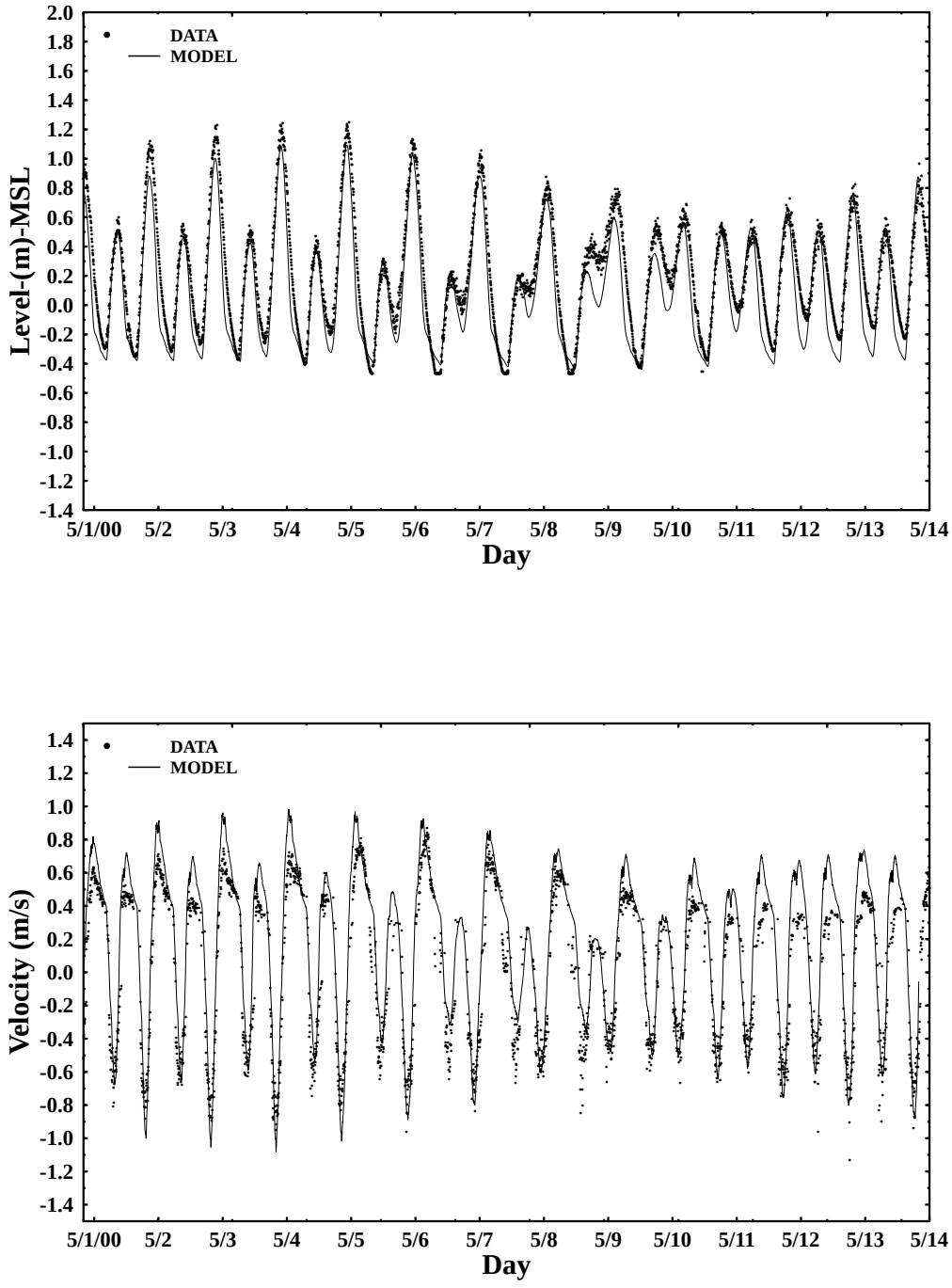

Figure 2. Comparison between predicted and measured water level (top) and velocity (bottom) at station PCH.

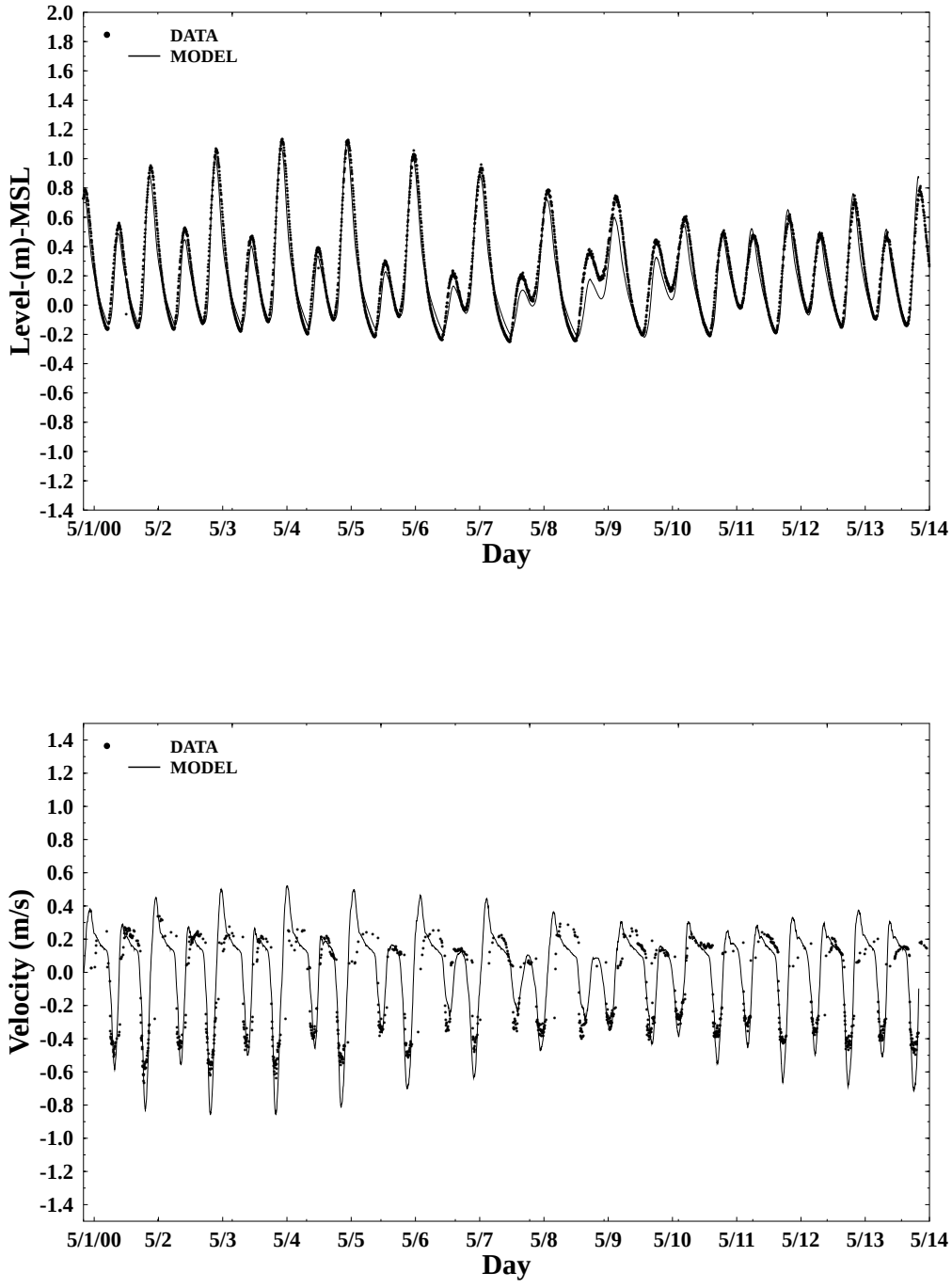

Figure 3. Comparison between predicted and measured water level (top) and velocity (bottom) at station BRK.

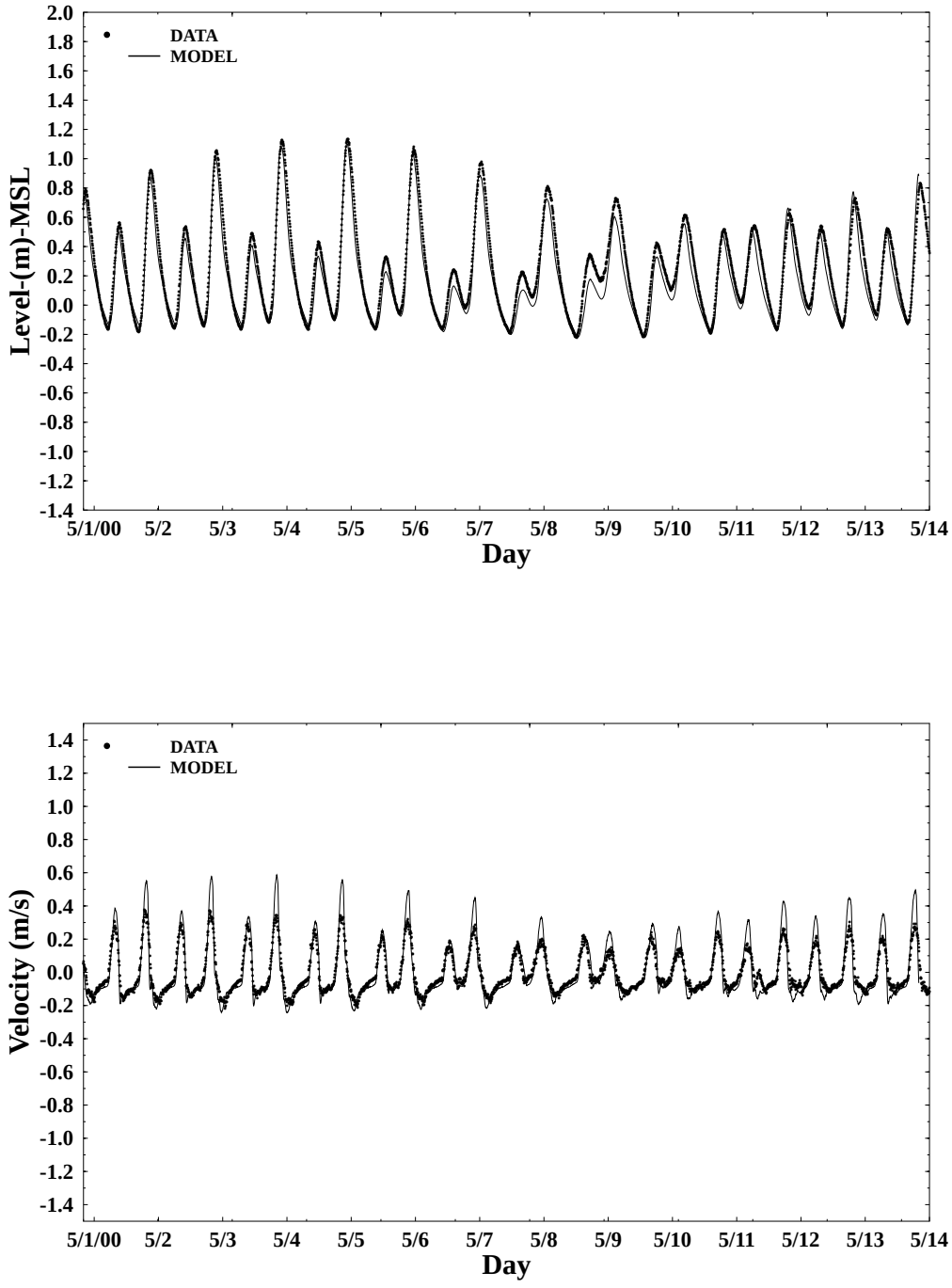

Figure 4. Comparison between predicted and measured water level (top) and velocity (bottom) at station AES.

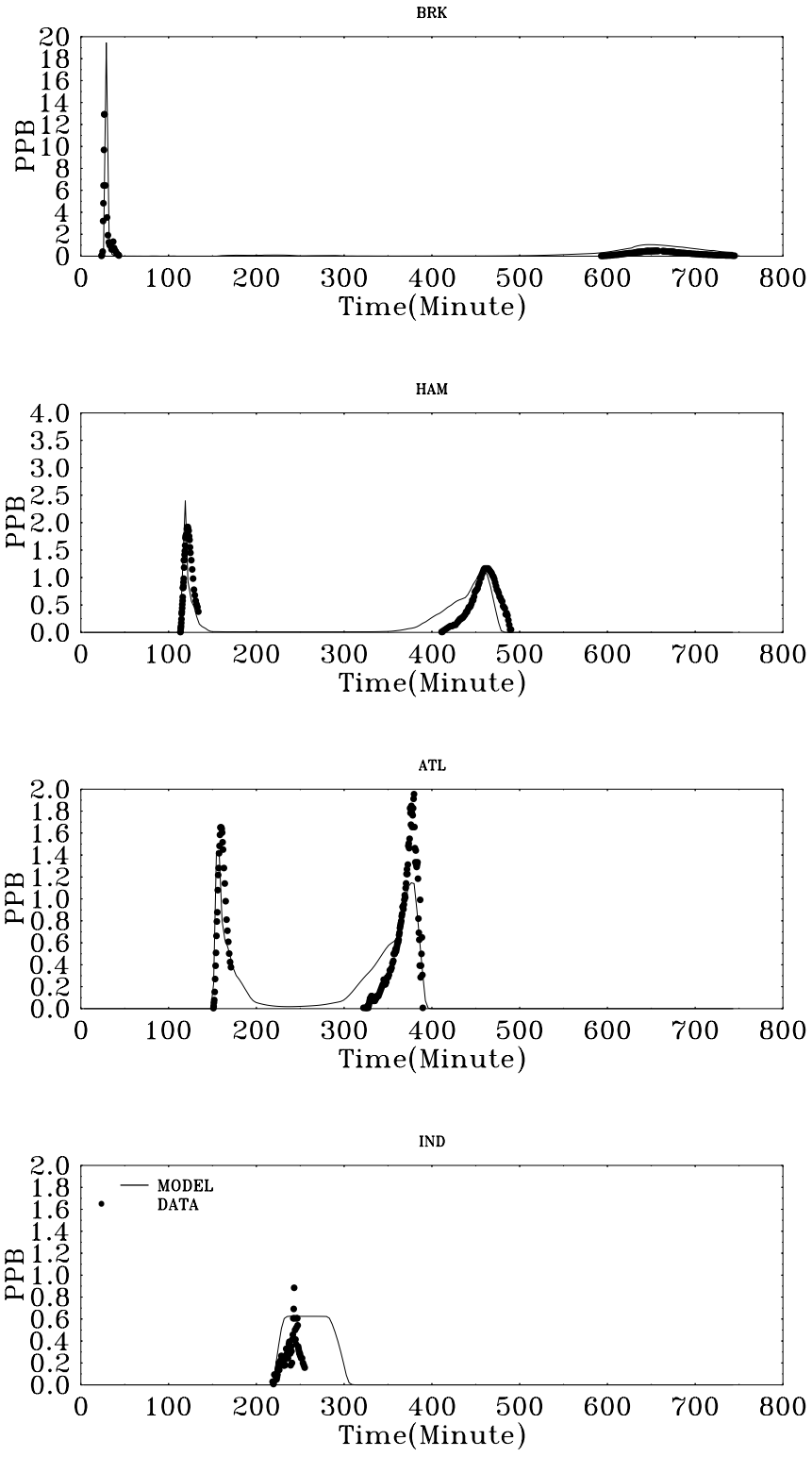

Figure 5. Comparison between predicted and measured dye concentrations.

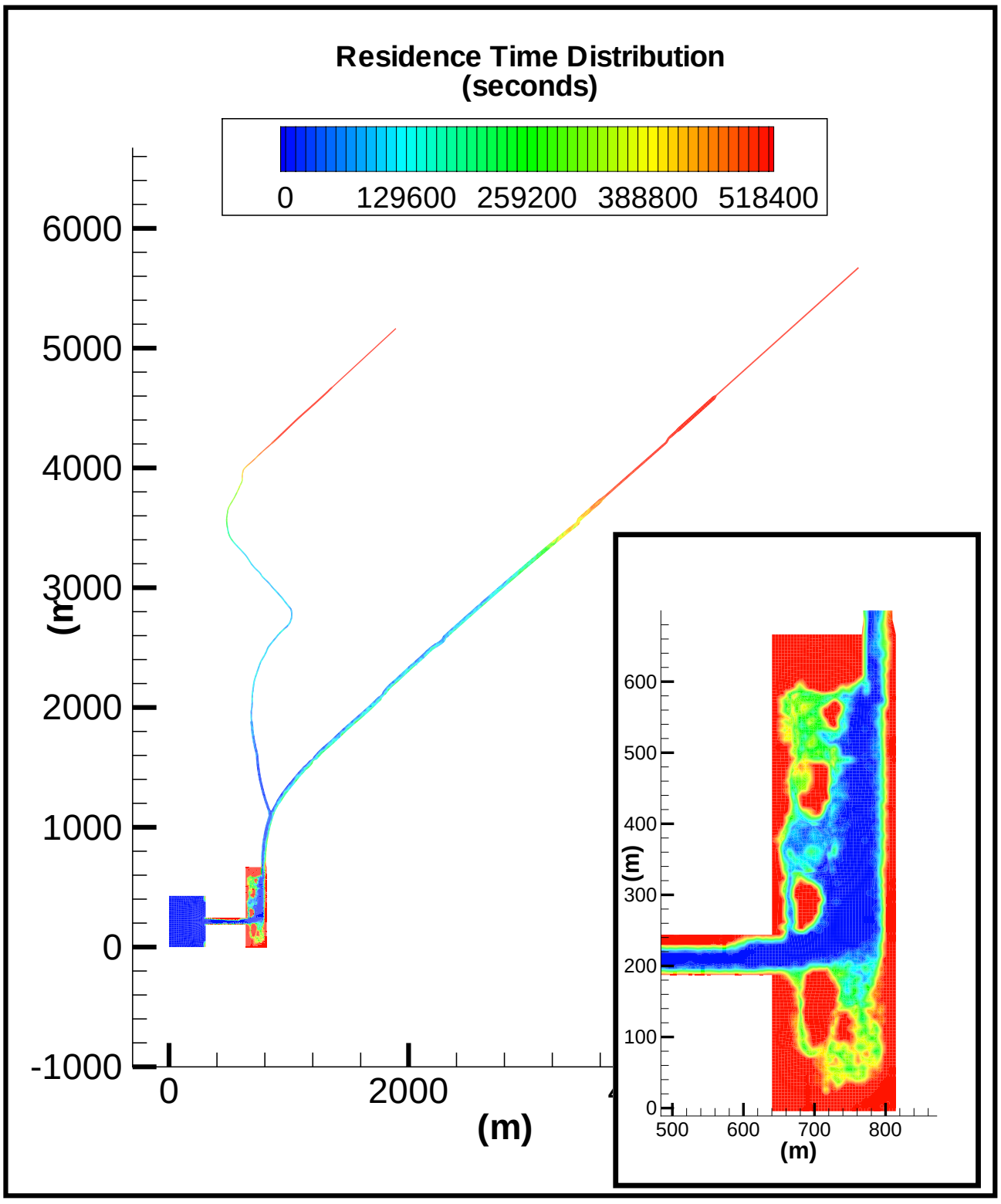

Figure 6. Residence time as a function of location within the channel and marsh network.

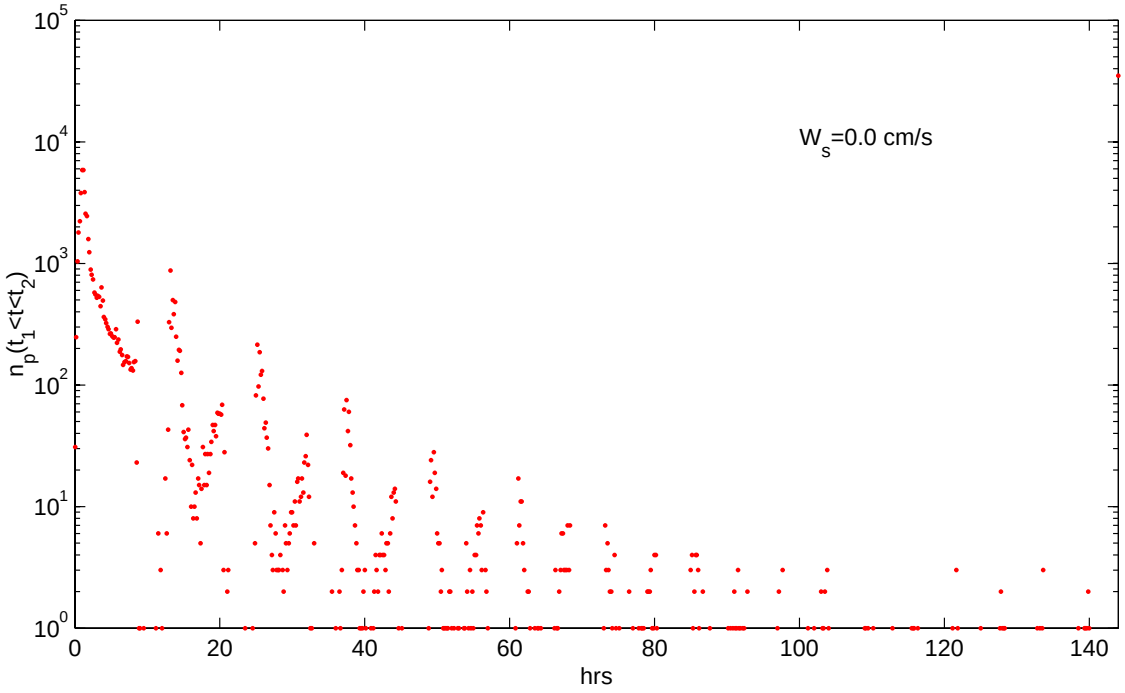

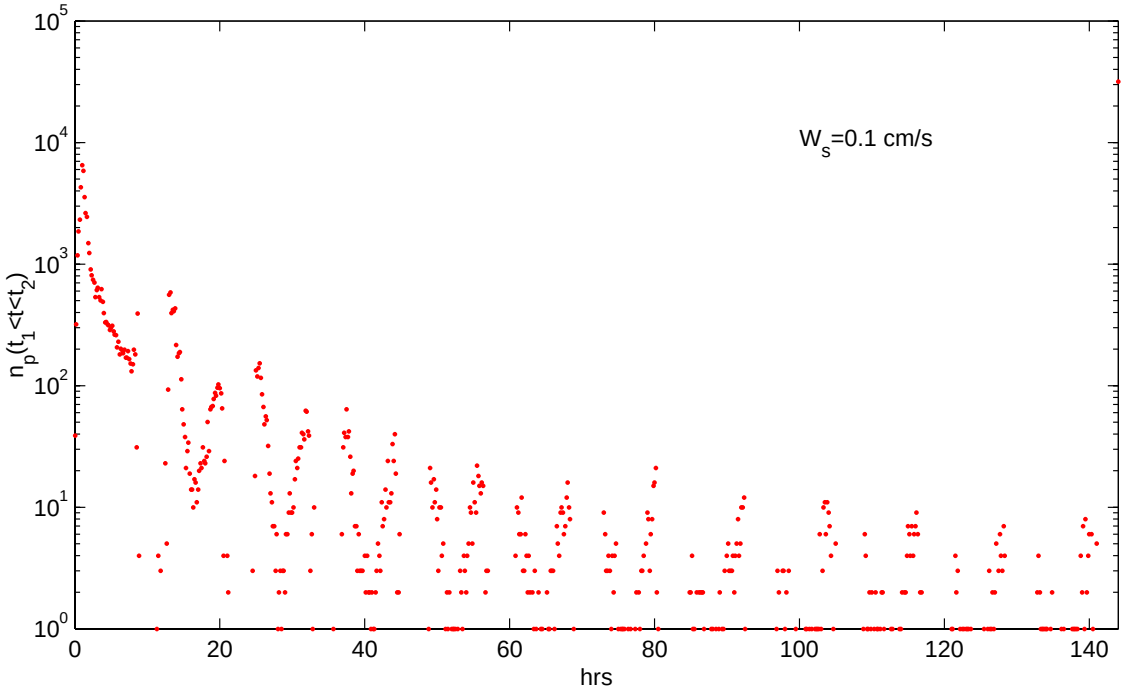

Figure 7. Residence time distribution for Ws=0 (top), and Ws=0.1 cm/s (bottom).